Journal of the Meteorological Society of Japan

EARLY ONLINE RELEASE

The DOI for this manuscript is
DOI:10.2151/jmsj.2024-019
J-STAGE Advance published date: March 1st, 2024

Diurnally propagating precipitation features caused by MCS activities during the pre-summer rainy season in South China

Yilun Chen[1,2], Aoqi Zhang[1,2], Tianao Liu[1], and Weibiao Li[1,2]

1School of Atmospheric Sciences and Key Laboratory of Tropical Atmosphere-Ocean System, Ministry of Education, Sun Yat-Sen University, Zhuhai, China

2Southern Marine Science and Engineering Guangdong Laboratory (Zhuhai), Zhuhai, China

----

1) Corresponding author: Aoqi Zhang, Sun Yat-sen University, Zhuhai, China

Email: zhangaoq3@mail.sysu.edu.cn

Tel: +86-156-0560-4905

Abstract

The impact of the directional propagation of mesoscale convective systems (MCSs) on precipitation structures during the pre-summer rainy season in South China remains unclear. Using multi-satellite datasets, this study aims to reveal the features and mechanisms of precipitation influenced by MCS propagation from the perspective of both cloud microphysics and diurnal forcing of land-atmospheric system. The study region mainly consists of three contiguous coastal regions (A1, B1, and C1 from southwest to northeast). Controlled by the steering flow, MCSs tend to move from region A1 to C1 with direction parallel to the coastline with a speed of 50 km h^{-1}. Although region A1 and C1 are both hilly regions, the results show that region A1 is the only key region for initiation and development of MCS, while MCSs in region C1 mainly come from the upstream regions. The directional propagation of MCS causes the propagation of diurnal rainfall peaks, while strong precipitation may accelerate the dissipation of MCS in region C1. The activities of MCSs enhanced ice-phased precipitation processes by spreading more droplets and therefore near-surface rainfall in region B1 and C1, whereas the hilly surface in region C1 further promoted liquid-phased processes by uplifting southerly low-level flow. Of all the thermodynamic parameters, the daytime vertically moistest layer above the boundary layer over the coastal regions plays a key role in the initiation and

development of MCS. These results contribute to a deeper understanding of MCS-related precipitations over coastal regions.

Keywords MCS; precipitation; propagation; coastal regions; diurnal forcing of land-atmospheric system

1. Introduction

The life cycle of precipitating cloud is resulted from complex atmospheric thermodynamics and cloud microphysical processes (Houze, 2014). These atmospheric thermodynamics are very complex including wind shear, terrain dynamics, lift of synoptic system, surface-atmospheric radiation, and latent heat changes (Ooyama, 2001). The microphysical processes involve nucleation, phase transition and collision-coalescence growth of cloud particles, as well as deposition, riming, aggregation, melting, and evaporation of precipitation droplets (Rosenfeld et al., 2008; Li and Shen, 2013). A comprehensive understanding of the evolution and mechanisms of precipitating clouds under the combined influences of these processes is crucial for comprehending the atmospheric water cycle and global energy balance (Oki and Kanae, 2006). Therefore, it has become a primary focus of research in meteorology.

Among the various atmospheric thermodynamics, the diurnal forcing of the land-atmospheric system driven by solar radiation has a direct impact on precipitating clouds, resulting in universal diurnal cycle of cloud and precipitation (Li et al., 2008; Zhou et al., 2008; Chen et al., 2009). Early numerical simulations showed that the diurnal variation of low clouds is mainly influenced by changes in saturation vapor pressure, whereas the diurnal variation of high clouds over land areas is mainly controlled by atmospheric instability (Bergman, 1997). During the East Asian summer monsoon, the diurnal variation of precipitation over most regions in South China peaks at afternoon because of surface heating (Yu et al., 2007), which is consistent with most land areas worldwide (Nesbitt and Zipser, 2003). On the opposite, the diurnal peak of precipitation in coastal areas often occurs in the morning due to the influence of land-sea thermal contrast (Cui, 2008; Chen et al., 2018).

Specifically, under the diurnal forcing of land-atmospheric system, the diurnal variation of precipitation clouds sometimes exhibits interesting propagation features (Carbone et al., 2002). For instance, the diurnal variation of summer precipitation in the Yangtze River valley shows a characteristic eastward propagation, with peak rainfall occurring from midnight to morning for upper to lower reaches of the Yangtze River (Wang et al., 2004; Zhang et al., 2019). Influenced by the sea-breeze circulation, cold cloud with precipitation continuously shifts inland throughout the night and then moves seaward throughout the morning during DJF over the Indonesian Maritime Continent (Marzuki et al., 2013). The daily rainfall peak over the Himalayas propagates from midnight to early morning in the slopes and foothills affected by the nighttime downslope flow (Pan et al., 2021). The directional propagation of clouds further influences the micro-properties of cloud and precipitation along the propagation paths (Chen et al., 2020; Zhang et al., 2022a). Therefore, revealing of propagative properties of precipitating clouds and their relevant mechanisms are important for high-resolution studies and predictions of regional precipitation.

The pre-summer rainy season in South China, which lasts from April to June, is a critical period for studying monsoon precipitating clouds, as it accounts for 40% to 60% of the regional total annual precipitation (Luo et al., 2017; Sun et al., 2019). Previous studies indicated that the Mesoscale Convective Systems (MCSs), known the largest of the convective storms (Houze, 2004), propagate with a speed of approximately 50 km h^{-1} towards the northeast along the coast during the pre-summer rainy season in South China (Li et al., 2020). Considering that numerous precipitations in South China are related to MCSs (Luo et al., 2017; Zhang and Meng, 2018; Shen et al., 2020; Zhang et al., 2023), such propagation feature could reflect on the diurnal variation of precipitation. In fact, previous studies have also investigated the diurnal propagation of precipitation in South China from other perspectives. For instance, Fang and Du (2022) revealed that the diurnal rainfall offshore propagation exists across ~78% of all coasts caused by inertia–gravity waves due to the land–sea thermal contrast, including the coasts of South China (Du and Rotunno, 2018). However, due to the steering flow, MCSs tend to move along the coast rather than seaward or landward (Zhang et al., 2022a). The impacts of MCS movement on diurnal propagation of precipitation in South China need further investigation.

In this context, this paper aims to address the above issue from the perspective of the interaction of the diurnal forcings of land-atmospheric system and cloud microphysics. Multiple observations including cloud-top information from Himawari-8 Advanced Image (AHI), 3-D precipitation microphysics from Global Precipitation Measurement (GPM) Dual-frequency Precipitation Radar (DPR), as well as gridded precipitation and reanalysis products were used in this study. The study mainly consists of three sections. Section 3.1

illustrates the propagation signals of MCS and rainfall; section 3.2 elucidates the impact of MCS propagation on precipitation microphysics; section 3.3 discusses the inner mechanisms.

2. Data and Method

2.1 Data usage

The MCS information used in this study was obtained from Advanced Himawari Image (AHI) equipped on Himawari-8 satellite. The AHI works at 16 bands with wavelength from 0.46 to 13.3 μm and spatial resolution from 0.5 to 2 km (Bessho et al., 2016). Among those bands, the 10.4 μm band is a split-window channel and can well reflect the temperature information of cloud top or surface. We used the 10.4 μm brightness temperature on $0.05^{o} \times 0.05^{o}$ grids with a temporal interval of 10 minutes (http: //ftp.ptree.jaxa.jp). Following the Mapes and Houze (1993), MCS was defined as connected grids with brightness temperature less than 235 K, which indicates ice-phased cloud top. In addition, the threshold of brightness temperature can be different in many other studies depending on its usage. For instance, Marzuki et al. (2017) used a threshold of 210 K to fit the average rainfall estimated by X-Band Doppler Radar. We used an eight-domain recognition algorithm to identify MCSs (Chen et al., 2019; Feng et al., 2021), in which adjacent pixels (from eight direction) with brightness temperature less than 235 K belong to the same MCS.

Two types of precipitation products provided by GPM were used in this study. One is the GPM dual-frequency precipitation radar (DPR) level-2 orbital product 2ADPR. GPM DPR consists of a Ku-band (KuPR, 13.6 GHz) and a Ka-band radar (KaPR, 35.5 GHz). The GPM 2ADPR data can provide users with 3-D precipitation observations including corrected reflectivity, rain type, rain rate, and DSD information with horizontal resolution of ~5 km and vertical interval of 125 m based on a series of dual-frequency algorithms (Iguchi et al., 2012; Hamada et al., 2016). Since GPM DPR operates at a low orbit of ~407 km above the Earth's surface, it usually covers the same location from 67°S to 67°N only 1–2 times per day.

Considering the sample size required for studying the diurnal variations of precipitation, another precipitation product called the Integrated Multi-satellite Retrievals for the GPM (IMERG) was also used in this study. IMERG is the GPM level-3 gridded precipitation product on 0.1° × 0.1° grids with temporal interval of 0.5 h. It provides users with calculated rain rates from multiple satellite visible–infrared and microwave sensors together with rain-gauge observations. The quality index of IMERG is high over the South China due to abundant rain gauges and validate microwave estimates (Huffman et al., 2015).

For consistency in this study, all valid precipitation pixels from either GPM 2ADPR or IMERG were restricted as larger than 0.5 mm h^{-1}. Precipitation consists of MCS-related and MCS-unrelated precipitation. Precipitation pixel was thought to be related to MCS if they are closer than 50 km. Specifically, the threshold, whether it is 0, 50, or 100 km, does not affect the main results of this study.

The latest ERA5 reanalysis dataset provided by the European Centre for Medium-

Range Weather Forecasts (ECMWF) was also used in this study (Hersbach et al., 2020). The ERA5 dataset provides wind, temperature, and geopotential on 37 pressure levels from surface to top of atmosphere with horizontal resolution of 0.25° and temporal interval of 1 h.

2.2 Focused area

To ensure data consistency, this study opted for the pre-summer rainy season in South China, from April to June, spanning five years (2016–2020). The 925 hPa wind in the coastal and adjacent ocean areas of South China presented consistently southerly winds, with an approximate speed of 3 m s^{-1} (Fig.1c). This finding suggests that the South China Sea is the primary source of moisture transport in this region. Due to the presence of the western Pacific subtropical high (indicated by the 5880 m contour), the 500 hPa wind field near the study region showed a southwest-to-northeast orientation, almost parallel to the coastline, with a speed of ~10 m s^{-1} (Fig. 1d). Since the MCSs and associated cloud clusters are typically distributed at altitudes ranging from approximately 4–10 km, we contend that the 500 hPa (~5.8 km) wind direction can indicate the direction of steering flow for MCS (Carbone et al., 2002; Li et al., 2020). Therefore, the MCS should move from southwest to northeast along the coastline.

Based on the direction of moisture transport, the direction of MCS movement, and the underlying surface conditions, the study area was delimited using six adjacent parallelograms as depicted in Fig. 1a. Among the three land regions (A1, B1, and C1), A1 and C1 are hilly regions and thought to be two key regions for convective initiation (Bai et al., 2020); region B1 indicates the Pearl River Delta Plain. Regions A2, B2, and C2 are the corresponding nearshore waters. Despite the decreasing trend of specific humidity from southwest to northeast over land (A1–C1; Fig. 1c), the average rainfall showed an increasing trend from 0.3 mm h^{-1} to 0.45 mm h^{-1} (Fig. 1b), which should be linked to the transport of hydrometeors caused by MCS movement. In the ocean regions, the average rainfall also showed an increasing trend from 0.1 mm h^{-1} in the west of A2 to 0.4 mm h^{-1} in the center of C2 along the direction of MCS movement (Fig. 1b).

The preliminary statistical analysis suggests that the interregional transport of hydrometeors caused by the propagation of MCS plays a crucial role in the formation and development of precipitation in the study area. Therefore, it is of significant scientific value to conduct further quantitative investigations on this topic.

3. Results

3.1 Propagation signals of MCS and rainfall

Firstly, we identified MCS with a threshold of <235 K, and calculated the latitude-mean diurnal variation of MCS frequency and mean brightness temperature for both land and ocean regions (Fig. 2). Specifically, MCS frequency represents the proportion of MCS samples to total samples at each grid. Due to the operational interval of Himawari-8 AHI, the statistics do not contain data at 1040 LST and 2240 LST.

In the land regions, the period of 08–16 LST was crucial for MCS development due to solar heating; Therefore, MCSs always reached their maximum area at around 16 LST; The maximum MCS area turned into the highest MCS frequency at around 16 LST (Fig. 2a). Along the meridional direction, the MCS frequency kept similar in Regions A1 and B1, while it decreased with increasing longitude in Region C1 during the peak period (10–22 LST). The pattern of MCS frequency in C1 showed a fishtail-like contraction with a slope of around 50 km h^{-1} (diagonal dashed line in Fig. 2a), consistent with the calculated movement speed of MCS using optical flow method and previous studies (Li et al., 2020; Zhang et al., 2022b). Together with the increasing brightness temperature of MCS in C1, we think that the environmental conditions, including abundant rainfall in C1, were relatively unfavorable for MCS development, leading to the gradual dissipation of MCS during its eastward movement (Fig. 2c). In addition, although the eastward propagation of MCS seems not obvious in the climatological scale of MCS frequency or brightness temperature over land (Fig. 2a & 2c), it did generally exist and can be clearly seen if we reduce the total time scale to 7 days or shorter (Fig. S1 in the supplementary file).

In contrast to the land regions, the ocean regions exhibited a lower overall occurrence frequency of MCS due to the lower rate of surface heating (Fig. 2a & 2b). The only prominent feature in ocean regions occurred in Regions B2–C2 at around 12–18 LST, indicating that more MCSs were formed in B2 around 12 LST and then propagated towards C2 with a speed of about 50 km h^{-1} (diagonal dashed line in Fig. 2b). The findings in Fig. 2 reveal significant eastward propagation characteristics of MCSs in the study area. The subsequent sections will focus on the changes in precipitation induced by MCS propagation.

In addition, the diurnal variations of MCS number and MCS area are showed in Fig. S2 in the supplementary file. They presented similar features to MCS frequency and mean brightness temperature (Fig. 2).

Similarly, we analyzed the latitude-mean diurnal variations of the total rainfall and contribution of MCS to total rainfall using the Himawari-8 and IMERG gridded product (Fig. 3). The diurnal variations of MCS-related rainfall are also presented in Fig. S3 in the supplementary file. Our results indicate that in the land regions, the diurnal rainfall peak occurred at around 16 LST (Fig. 3a), which corresponded well with the peak time of MCS frequency (Fig. 2a). The contribution of MCS activity to precipitation reached 90% at nearly all times over the land regions (Fig. 3c), suggesting that the diurnal rainfall peak was primarily caused by MCS activity. The latitude-mean diurnal rainfall peak showed two propagation bands at around 16 LST over the land regions, one from A1 to B1 and the other from B1 to C1 (Fig. 2a), indicating that new MCSs initiated in both the A1 and B1 regions. The propagation speeds of the two bands were both around 50 km h^{-1}, which was consistent with the moving speed of MCSs.

On the contrast, the diurnal variation of rainfall over the ocean regions peaked at around 08 LST (Fig. 3b). The MCS activity was relatively not active at that time (Fig. 2b), while still more than 90% rainfall was MCS-related rainfall (Fig. 3d). The diurnal propagation of rainfall was less obvious over the ocean regions (Fig. 3b) compared with the land regions.

Both the previous studies and our results showed that the propagation speed of MCS (or diurnal rainfall peak) was significantly larger than the steering flow (Li et al., 2020; Fig. 2&3). Here, to figure out the inner mechanism, we present a case analysis detected by GPM 2ADPR and Himawari-8 AHI. Specifically, this individual case was chosen for two main reasons. Firstly, this case was an MCS-related precipitation case and it was located at the front of MCS. Secondly, the occurring time of this event was consistent with the diurnal peak of rainfall. The rainfall area was not too small and the maximum rainfall intensity was high. As shown in Fig. 4, this precipitation event was characterized by two distinct precipitation centers in region B1 and C1, respectively. The maximum near-surface rain rate in both regions exceeded 10 mm h^{-1} (Fig. 4a). The precipitation center in region B1 was dominated by stratiform precipitation, while there exhibited numerous convective samples near the coastlines in region C1.

Figure 5 displays the half-hourly horizontal distributions of the MCS associated with the precipitation event, which was detected near the time of Fig. 5e. The MCS gradually shifted eastward over time, with the core region of lowest brightness temperature shifting from the center of A1 at 1410 LST to the east of B1 at 1810 LST (Fig. 5). During the 4-hour period, the MCS moved approximately 200 km with a speed of 50 km h^{-1} (consistent with the statistics). Prior to the time of DPR swath, the MCS area gradually increased while the minimum brightness temperature kept below 215 K, indicating that the MCS was in the mature stage (Fig. 5a–e). After the time of DPR swath, the MCS area gradually decreased and the minimum brightness temperature gradually increased, indicating that the MCS was in the dissipation stage (Fig. 5e–i). Consequently, the DPR precipitation event occurred during the transition stage from mature to dissipation. It takes abundant from MCS and may further accelerate the dissipation of the MCS.

It is noteworthy that new convective cores were continuously generated ahead of the moving MCS (Fig. 5). Similar phenomena have been extensively reported in the literature, which were associated with the reverse updrafts and moist adiabatic instability ahead of the storm motion (Kingsmill and Houze, 1999). These phenomena provide a reasonable explanation for the significantly faster propagation of MCSs compared to the steering flow (< 20 m s^{-1}).

3.2 Microphysics within precipitation

In this section, we will utilize the dual-frequency detections from GPM 2ADPR to examine the 3-D characteristics of precipitation in the study area. The aim is to uncover the possible impact of MCS propagation on precipitation microphysics. During the pre-summer rainy season in South China, GPM 2ADPR detected a total of 5135, 7427, and 5461 precipitation pixels in Regions A1, B1, and C1 (land), as well as 2326, 3902, and 4008 precipitation pixels in Regions A2, B2, and C2 (ocean). Among them, there were respectively 3260, 6352, 4262, 1405, 2914, and 3305 precipitation samples related to MCS. Due to the relatively small number of precipitation samples, we will solely perform statistics within each overall region, instead of using the latitude average as in section 3.1 and 3.3.

The Probability Density Functions (PDFs) of near-surface rain rate for precipitations related to MCS activity are showed in Fig. 6a and 6b. The total rainfall, average near-surface rain rate, and the proportion of heavy rainfall gradually increased from A1 to C1 (Fig. 3a & 6a). It is because the atmospheric precipitable water gradually accumulated in the form of cloud water with the development of eastward movement of MCS. From region A1 to C1, weak precipitations with rain rate < 2 mm h^{-1} accounted for 62.1%, 42.6%, and 41.6% of the total samples, while heavy precipitation with rain rate > 10 mm h^{-1} accounted for 5.62%, 11.6%, and 14.3% of the total samples, respectively. Over the ocean regions from A2 to C2 (Fig. 6b), weak precipitation accounted for 53.2%, 41.9%, and 44.6% of the total samples, while heavy precipitation accounted for 10.5%, 10.3%, and 14.0% of the total samples, respectively.

As for the PDFs of storm-top height (STH), a bimodal distribution with peaks at 6 km and 11.5 km was observed only in A1, while the other land regions exhibited a unimodal distribution around 6 km (Fig. 6c). We attributed it to that numerous MCSs in A1 were newly born and still in developing stage, with high cloud tops and rain tops (Zhang and Fu, 2018). Over the ocean regions, there was a gradual increasing trend in STH from A2 to C2 (Fig.6d). High precipitation samples with STH > 10 km accounted for 16.2%, 22.9%, and 27.3% of the total precipitation samples in A2, B2, and C2, respectively.

The Contoured Frequency by Altitude Diagram (CFAD) analysis is a useful tool to investigate the vertical structure of precipitation (Houze et al., 2007). For land regions, the CFAD of A1 showed a bimodal distribution with peaks at 7 km and 12.5 km (Fig. 7a), which corresponded to the bimodal distribution of STH (Fig. 6c). We attributed the higher peak to numerous newly triggered MCS. The ice-phased reflectivity was more prominent in B1 and C1 than in A1 due to the eastward movement of existing MCS (Fig. 7a–7c). The enhanced ice-phase precipitation processes in B1 and C1 led to stronger echo intensity near the freezing layer, resulting in a significant reduction in the proportion of weak precipitation. Moreover, the CFAD of MCS-related precipitation in C1 showed a more dispersed distribution compared to B1, particularly below melting layer (Fig. 7b & 7c). This implied more active liquid-phased processes in C1, leading to a higher proportion of heavy precipitation (Fig. 6a).

For the ocean regions, the ice-phased reflectivity was quite weak in region A2, suggesting it may originate from the edge areas of MCSs (Fig. 7d). By contrast, the ice-phased reflectivity was much stronger in B2 and C2 (Fig. 7d–f), consistent with higher MCS frequency (Fig. 2b). The distribution pattern of CFAD in region C2 was wider than that in B2, with higher potential STH and near-surface reflectivity. Moreover, the top of CFAD in C2 exhibited a double peak (Fig. 7f), indicating the generation of new MCSs.

We further calculated the average profiles of Droplet Size Distribution (DSD) for MCS-related precipitation (Fig. 8). The most prominent feature is that dBN_w gradually increased from southwest to northeast over land regions (A1–C1; Fig. 8a). The increase of dBN_w from A1 to B1 mainly occurred in the altitude of 5 km, indicating that the existing MCS spread more droplets during its development and eastward movement. By contrast, the increase of dBN_w from B1 to C1 mainly occurred from 7 km to near-surface, suggesting the generation of numerous new precipitation droplets due to ice-phased rime splintering process and liquid-phased collision process.

The D_m profiles over three land regions showed intersection at around 6 km (Fig. 8c). Above 6 km, precipitation droplets were averagely larger in region A1 than in B1 or C1, which is related to the higher generation height of precipitation droplets during the initiation and developing stage of MCS. Correspondingly, the growth rate of D_m with decreasing height was significantly faster in region B1 or C1 than in A1, indicating more active ice-phased riming and aggregation processes. Due to the generation of new droplets, the D_m in region C1 was similar to B1 above 6 km, while lower than B1 below 6 km.

In addition, given that both A1 and C1 are hilly regions while B1 is plain, the monotonical increase of dBN_w from A1 to C1 is less likely to be affected by terrain. We still think that the terrain does affect the microphysics of MCS-related precipitation, but it was less important than the propagation of MCS. In our opinion together with the results in the following section, the hilly surface in A1 promoted the atmospheric instability and therefore was favor for MCS development; the hilly surface in C1 increased updraft, which leads to the leading to the fragmentation of liquid-phased precipitation droplets (larger dBN_w and smaller D_m below melting layer).

For ocean regions, the overall characteristics of DSD profiles were similar to their corresponding land regions, but with smaller regional differences in magnitude (Fig. 8b & 8d). Moreover, the regional differences among ocean regions were also due to the ice-phased processes above 6 km, indicating existing MCS spread more droplets with development and eastward movement. D_m was averagely the largest in region B2, while the smallest was in B1; the difference was also influenced by the riming and aggregation processes. These findings highlight the crucial role of the ice-phase processes in the MCS-related precipitation over the ocean regions.

3.3 Diurnal forcings of land-atmospheric system

Cloud and precipitation result from the interactions between atmospheric thermodynamics and cloud microphysical processes (Houze, 2014). For a better understanding of the revealed diurnal variation and microphysics of MCS-related precipitation in the previous sections, we will try to reveal the key atmospheric thermodynamics from the perspective of diurnal forcing.

The diurnal variation of relative humidity plays a key role in the triggering and development of MCS (Bergman, 1997). Figure 9 illustrates the two-dimensional distributions of relative humidity on local time and longitude over the land and ocean regions. The most prominent feature of relative humidity over land is that a vertically moist layer existed near the surface during nighttime while it exhibited above the Planetary Boundary Layer (PBL) top during daytime (Fig. 9a–c).

Fig. 10 presents the conceptual models for the variation of the moistest layer. During nighttime when the atmospheric layer was stable, the relative humidity decreased with increasing height (Fig. 10a). During daytime over the land regions (Fig. 10b), on the one hand, strong surface heating within PBL led to the increase of saturation vapor pressure and the decrease of relative humidity with increasing height within PBL (Fig. 9a–c). On the other hand, the depth of PBL increased more over land than ocean. Thus, the water vapor content above the PBL came from lower oceanic atmosphere during daytime compared to the nighttime, which increased the relative humidity over the PBL top (Fig. 10b). This led to the presence of a prominent moist layer above the PBL during daytime, which favored the formation and development of MCS. In addition, the moisture layer was significantly deeper with longer duration in Region A1 than in B1 or C1 (Fig. 9a–c), consistent with the key role of region A1 in MCS initiation.

For the ocean regions, the regional differences of relative humidity were mainly observed at the height of 900–700 hPa, which was more prominent during nighttime (Fig. 9d–f). The increased relative humidity from A2 to C2 was favorable for precipitation and might be linked with the reverse moistening by the eastward propagation of MCS.

Due to the diurnal reverse of sea-land breezes circulation, the vertical velocity exhibited peak values over land regions at 16 LST (Fig. 11a–c), which were consistent with the peak times of MCS and precipitation (Fig. 2 & 3). Among the land regions, the upward velocity at 16 LST was the strongest in region A1, followed by C1, and the weakest in B1. The sort of upward velocity at 16 LST is caused by two aspects with different impact on MCS and precipitation. The first one is that the moist layer above PBL increased the atmospheric instability, showed as decreasing θ_e with height (Fig. 11a–c), which was the highest in region A1 and favored the development of MCS. The other one is that the hilly surface lifted the southerly low-level flow and promoted updraft.

The atmospheric layer was more stable in ocean regions compared to that in the continental regions (Fig. 11). The diurnal peaks of updraft and rainfall occurred respectively at nighttime (04 LST) and early morning (08 LST) over the ocean regions (Fig. 3b & Fig. 11d–f), showing the importance of cloud-top radiation cooling for the development of MCS and precipitation. The time lag between updraft and rainfall may be attributed to the temporal sequence of radiation cooling, cloud development (release latent heat), updraft, intensified convection, and finally precipitation. In addition, due to the convergence forced by the friction between low-level flow and underlying surface, the updraft existed at nearly all time in the study region and brought heavy rainfall near the coastline (Fig. 1b & 11).

4. Conclusion and Discussion

The life-cycle evolution of precipitating clouds plays a vital role in the atmospheric water cycle, and is directly affected by the diurnal forcing of land-atmosphere system driven by solar radiation. Using high-resolution cloud, precipitation, and environmental datasets, this study aims to reveal the features and mechanisms of precipitating clouds over the coasts of South China influenced by the directional propagation of MCS. Both cloud microphysics and diurnal forcing of land-atmosphere system are analyzed in this study; and the main findings are discussed below.

The selected research regions consist of three contiguous coastal regions (A1–C1) as well as three corresponding offshore area (A2–C2). During the study period in the pre-summer rainy season from 2016 to 2020, the atmospheric moisture flux was mainly southerly at lower layers from South China Sea as a result of the Eastern Asia summer monsoon. Driven by the steering flow at mid-high layers of atmosphere, MCSs tended to move from A1(A2) to C1(C2) with routines parallel to the coasts. The speed of MCS (~50 km) far exceeded the steering flow as reported in previous studies (Li et al., 2020), which we think may be due to continuously generated convective cells ahead of moving MCS.

Over the coastal regions, MCS activities contributed more than 70% of the total rainfall. A1 and C1 had similar surface type of hills, and were reported to be the two key regions for convective initiation of warm-sector heavy rainfall (Bai et al., 2020). However, our results suggested that only A1 was the key region for convective initiation, while MCSs over C1 mainly came from upstream rather than initiated locally. The MCS frequency kept similar over A1–B1 while it decreased sharply in C1; and the brightness temperature of MCS increased from B1 to C1. MCSs would like to initiate over A1 due to the vertically moistest layer above PBL and the most unstable atmospheric layer. It soon propagated eastward to B1 and transformed into mature stage. MCSs would begin to dissipate over C1 with heaviest precipitation.

It is found that the diurnal propagation of MCS had a huge impact on precipitation characteristics over the coastal regions of South China. Firstly, it caused the propagation of diurnal rainfall peaks over A1–B1 and B1–C1 with propagation speed the same as MCS speed. Similar diurnal propagation features due to MCSs were also shown by previous studies over the Yangtze River and the Himalayas (Wang et al., 2004; Pan et al., 2021), indicating it can exist widely in the world. Secondly, the propagating MCS from upstream brought large amounts of cloud water and strengthened the ice-phased processes of precipitation. Therefore, both the total rainfall and the droplet density above freezing layer increased sharply from A1 to C1 despite the decreasing low-level specific humidity. Thirdly, the surface type also played a key role in the MCS-related precipitation microphysics. The hilly surface in Region C1 led to a more pronounced land-sea contrast conditions compared to B1. This, in turn, lifted the southerly low-level flow, leading to the generation of numerous new precipitation droplets in the mid-to-low levels in C1. Consequently, the droplet density was higher in C1 compared to B1, while the average droplet size was smaller in C1.

Over the offshore regions, the MCS frequency, as well as its contribution to total rainfall, was much lower than the coastal regions. The nighttime cooling played a rather important role in formation of MCS and precipitation. The influence of MCS propagation on precipitation was less obvious compared to coastal regions. Because the underlying surfaces and environmental conditions were similar among A2–C2, the moderate variations in MCS-related precipitation primarily arose from the ice-phase precipitation processes rather than liquid-phase precipitation processes.

Data Availability Statement

The GPM 2ADPR and IMERG precipitation data was collected from the Precipitation Measurement Mission website (https://pmm.nasa.gov). The Himawari-8 AHI L1 brightness temperature information was provided by the Japanese Meteorological Agency (http://www.data.jma.go.jp/mscweb/en/himawari89/). The ERA5 reanalysis data was collected from the ECMWF website (https://apps.ecmwf.int/).

Acknowledgments

This research was funded by the Guangdong Major Project of Basic and Applied Basic Research (grant number 2020B0301030004), the National Natural Science Foundation of China (Grant 42105068), the Open Project Fund of China Meteorological Administration Basin Heavy Rainfall Key Laboratory (Grant 2023BHR-Z04), and the Innovation Group Project of Southern Marine Science and Engineering Guangdong Laboratory (Zhuhai) (Grant number 311022006).

References

Bai, L., G. Chen, and L. Huang, 2020: Convection Initiation in Monsoon Coastal Areas (South China). *Geophys. Res. Lett.*, **47**, e2020GL087035, doi: 10.1029/2020GL087035.

Bergman, J. W., 1997: A Numerical Investigation of Cloud Diurnal Variations. *J. Climate*, **10**, 2330-2350.

Carbone, R. E., J. D. Tuttle, D. A. Ahijevych, and S. B. Trier, 2002: Inferences of Predictability Associated with Warm Season Precipitation Episodes. *J. Atmos. Sci.*, **59**, 2033-2056.

Chen, D., J. Guo, D. Yao, Y. Lin, C. Zhao, M. Min, H. Xu, L. Liu, X. Huang, T. Chen, and P. Zhai, 2019: Mesoscale Convective Systems in the Asian Monsoon Region from Advanced Himawari Imager: Algorithms and Preliminary Results. *J. Geophys. Res.: Atmos.,* **124**, 2210-2234.

Chen, G., W. Sha, and T. Iwasaki, 2009: Diurnal variation of precipitation over southeastern China: Spatial distribution and its seasonality. *J. Geophys. Res*. **114**, D13103, doi:10.1029/2008JD011103.

Chen, G., R. Lan, W. Zeng, H. Pan, and W. Li, 2018: Diurnal Variations of Rainfall in Surface and Satellite Observations at the Monsoon Coast (South China). *J. Climate*, **31**, 1703-1724.

Chen, Y., A. Zhang, Y. Zhang, C. Cui, R. Wan, B. Wang, and Y. Fu, 2020: A Heavy Precipitation Event in the Yangtze River Basin Led by an Eastward Moving Tibetan

Plateau Cloud System in the Summer of 2016. *J. Geophys. Res.*: *Atmos.*, **125**, e2020JD032429, doi: 10.1029/2020JD032429.

Cui, X., 2008: A cloud-resolving modeling study of diurnal variations of tropical convective and stratiform rainfall. *J. Geophys. Res.* **113**, D02113. doi:10.1029/2007JD008990.

Fang, J., and Y. Du, 2022: A global survey of diurnal offshore propagation of rainfall. *Nat. Commun*., **13**, 7437 (2022), doi:10.1038/s41467-022-34842-0.

Feng, Z., L. R. Leung, N. Liu, J. Wang, R. A. Houze, J. Li, J. C. Hardin, D. Chen, and J. Guo, 2021: A Global High-Resolution Mesoscale Convective System Database Using Satellite -Derived Cloud Tops, Surface Precipitation, and Tracking. *J.Geophys. Res.*: *Atmos.,* **126**, e2020JD034202, doi:10.1029/2020JD034202.

Hamada, A., and Y. N. Takayabu, 2016: Improvements in Detection of Light Precipitation with the Global Precipitation Measurement Dual-Frequency Precipitation Radar (GPM DPR). *J. Atmos. Oceanic Technol*., **33**, 653-667.

Hersbach, H., B. Bell, P. Berrisford, S. Hirahara, A. Horányi, J. Muñoz Sabater, J. Nicolas, C. Peubey, R. Radu, D. Schepers, A. Simmons, C. Soci, S. Abdalla, X. Abellan, G. Balsamo, P. Bechtold, G. Biavati, J. Bidlot, M. Bonavita, G. Chiara, P. Dahlgren, D. Dee, M. Diamantakis, R. Dragani, J. Flemming, R. Forbes, M. Fuentes, A. Geer, L. Haimberger, S. Healy, R. J. Hogan, E. Hólm, M. Janisková, S. Keeley, P. Laloyaux, P. Lopez, C. Lupu, G. Radnoti, P. Rosnay, I. Rozum, F. Vamborg, S. Villaume, and J. N. Thépaut, 2020: The ERA5 global reanalysis. *Quart. J. Roy. Meteor. Soc.,* **146**, 1999-2049.

Houze, R. A., 2004: Mesoscale convective systems. *Rev. Geophys.*, **42**, RG4003, doi:10.1029/2004RG000150.

Houze, R. A., D. C. Wilton, and B. F. Smull, 2007: Monsoon convection in the Himalayan region as seen by the TRMM Precipitation Radar. *Quart. J. Roy. Meteor. Soc.,* **133**, 1389-1411.

Houze, R. A., 2014: *Cloud Dynamics*. 2nd ed. Elsevier, 432 pp.

Huffman, G. J., D. T. Bolvin, D. Braithwaite, K. Hsu, R. Joyce, P. Xie, and S. Yoo, 2015: NASA global precipitation measurement (GPM) integrated multi-satellite retrievals for GPM (IMERG). *Algorithm Theoretical Basis Document (ATBD) Version*. **4**, 26.

Iguchi, T., S. Seto, R. Meneghini, N. Yoshida, J. Awaka, T. Kubota, T. Kozu, V. Chandra, M. Le, L. Liao, S. Tanelli, and S. Durden, 2012: An overview of the precipitation retrieval algorithm for the dual-frequency precipitation radar (DPR) on the global precipitation measurement (GPM) mission's core satellite. *Proc. SPIE*. **8528**, 85281C.

Kingsmill, D. E., and R. A. Houze, 1999: Thermodynamic characteristics of air flowing into and out of precipitating convection over the west Pacific warm pool. *Quart. J. Roy. Meteor. Soc.,* **125**, 1209-1229.

Li, G., F. Kimura, T. Sato, and D. Huang, 2008: A composite analysis of diurnal cycle of GPS precipitable water vapor in central Japan during Calm Summer Days. T*heor. Appl. Climatol*., **92**, 15-29.

Li, P., C. Moseley, A. F. Prein, H. Chen, J. Li, K. Furtado, and T. Zhou, 2020: Mesoscale

Convective System Precipitation Characteristics over East Asia. Part I: Regional Differences and Seasonal Variations. *J. Climate*, **33**, 9271-9286.

LI, X., and X. Shen, 2013: Rain Microphysical Budget in the Tropical Deep Convective Regime: A 2-D Cloud-Resolving Modeling Study. *J. Meteor. Soc. Japan,* **91**, 801-815.

Luo, Y., Q. Wan, B. Wang, W. K. Wong, Z. Hu, B. J. Jou, Y. Lin, R. H. Johnson, C. Chang, Y. Zhu, X. Zhang, H. Wang, R. Xia, J. Ma, D. Zhang, M. Gao, Y. Zhang, X. Liu, Y. Chen, H. Huang, X. Bao, Z. Ruan, Z. Cui, Z. Meng, J. Sun, M. Wu, H. Wang, X. Peng, W. Qian, K. Zhao, and Y. Xiao, 2017: The Southern China Monsoon Rainfall Experiment (SCMREX). *Bull. Amer. Meteor. Soc.*, **98**, 999-1013.

Mapes, B. E., and R. A. Houze, R. A., 1993: Cloud clusters and superclusters over the oceanic warm pool. *Mon. Wea. Rev.*, **121**, 1398-1415.

Marzuki, H. Hashiguchi, M. K. Yamamoto, M. Yamamoto, S. Mori, M. D. Yamanaka, R. E. Carbone, and J. D. Tuttle, 2013: Cloud episode propagation over the Indonesian Maritime Continent from 10 years of infrared brightness temperature observations. *Atmos. Res.,* **120-21**, 268-286.

Marzuki, M. Vonnisa, A. Rahayu, and H. Hashiguchi, 2017: Cloud statistics over the Indonesian Maritime Continent during the first and second CPEA campaigns. *Atmos. Res.,* **189**, 99-110.

Nesbitt, S. W., and E. J. Zipser, 2003: The diurnal cycle of rainfall and convective intensity according to three years of TRMM measurements. *J. Climate*, **16**, 1456-1475.

Oki, T., and S. Kanae, 2006: Global hydrological cycles and world water resources. *Science*, **313**, 1068-1072.

Ooyama, K. V., 2001: A dynamic and thermodynamic foundation for modeling the moist atmosphere with parameterized microphysics. *J. Atmos. Sci.*, **58**, 2073-2102.

Pan, X., Y. Fu, S. Yang, Y. Gong, and D. Li, 2021: Diurnal Variations of Precipitation over the Steep Slopes of the Himalayas Observed by TRMM PR and VIRS. *Adv. Atmos. Sci.,* **38**, 641-660.

Rosenfeld, D., W. L. Woodley, A. Lerner, G. Kelman, and D. T. Lindsey, 2008: Satellite detection of severe convective storms by their retrieved vertical profiles of cloud particle effective radius and thermodynamic phase. *J. Geophys.Res.*, **113**, D4208, doi:10.1029/2007JD008600.

Sun, J., Y. Zhang, R. Liu, S. Fu, and F. Tian, 2019: A Review of Research on Warm-Sector Heavy Rainfall in China. *Adv. Atmos. Sci*., **36**, 1299-1307.

Wang, C., G. T. Chen, and R. E. Carbone, 2004: A Climatology of Warm-Season Cloud Patterns over East Asia Based on GMS Infrared Brightness Temperature Observations. *Mon. Wea. Rev.,* **137**, 1606-1629.

Yu, R., T. Zhou, A. Xiong, Y. Zhu, and J. Li, 2007: Diurnal variations of summer precipitation over contiguous China. *Geophys. Res. Lett*., **34,** L01704, doi:10.1029/2006GL028129.

Zhang, A., and Y. Fu, 2018. Life Cycle Effects on the Vertical Structure of Precipitation in East China Measured by Himawari-8 and GPM DPR. *Mon. Wea. Rev*., **146**, 2183-2199.

Zhang, A., C. Chen, Y. Chen, W. Li, S. Chen, and Y. Fu, 2022: Resilient dataset of rain clusters with life cycle evolution during April to June 2016–2020 over eastern Asia based on observations from the GPM DPR and Himawari-8 AHI. *Earth Syst. Sci. Data*, **14**, 1433-1445.

Zhang, A., Y. Chen, X. Pan, S. Chen, W. Li, and Y. Fu, 2022: Entangled Impacts of Large-Scale Monsoon Flows and Terrain Circulations on the Diurnal Cycle of Rainfall over the Himalayas. *J. Atmos. Sci*., **79**, 301-316.

Zhang, M., and Z. Meng, 2018: Impact of Synoptic -Scale Factors on Rainfall Forecast in Different Stages of a Persistent Heavy Rainfall Event in South China. *J. Geophys. Res.*: *Atmos.,* **123**, 3574-3593.

Zhang, Y., M. Xue, K. Zhu, and B. Zhou, 2019: What Is the Main Cause of Diurnal Variation and Nocturnal Peak of Summer Precipitation in Sichuan Basin, China? The Key Role of Boundary Layer Low-Level Jet Inertial Oscillations. *J. Geophys. Res.*: *Atmos.,***124**, 2643-2664.

Zhou, T., R. Yu, H. Chen, A. Dai, and Y. Pan, 2008: Summer Precipitation Frequency, Intensity, and Diurnal Cycle over China: A Comparison of Satellite Data with Rain Gauge Observations. *J. Climate,* **21**, 3997-4010.

List of Figures

Fig. 1. Average distributions of (a) terrain height, (b) IMERG hourly rainfall, (c) ERA5 925 hPa specific humidity overlapped with wind field, and (d) ERA5 500 hPa geopotential height overlapped with wind field during the pre-summer rainy season (April-June) in 2016–2020. The six parallelograms indicate our study regions.

Fig. 2. Diurnal variations of (a–b) MCS frequency and (c–d) brightness temperature of MCS, averaged by latitude over the study regions derived from Himawari-8 AHI. The intervals of time and longitude are 1/6 hour and 0.05°, respectively.

Fig. 3. The contributions of (a–b) half-hourly rainfall to daily rainfall and (c–d) MCS to rainfall (attributed to MCS if within 50 km) averaged by latitude over the study regions. The intervals of time and longitude are 0.5 hour and 0.05°, respectively.

Fig. 4. Horizontal distributions of (a) near-surface rain rate and (b) rain type for an MCS-related precipitation event detected by GPM 2ADPR at 1613 LST, 5 June, 2016.

Fig. 5. Hourly distributions of Himawari-8 10.8 μm brightness temperature for the detected event. The DPR precipitation event occurred near the time of panel (e).

Fig. 6. PDFs of (a–b) near-surface rain rate and (c–d) STH for MCS-related precipitations detected by GPM 2ADPR during the pre-summer rainy season in 2016–2020. The interval of near-surface rain rate is constant in the log coordinate ($\Delta(\lg RR) = 0.1$), and the interval of STH is 0.25 km.

Fig. 7. CFADs of Ku-band reflectivity of MCS-related precipitations over the study regions during the pre-summer rainy season in 2016–2020. The intervals of height and reflectivity are 0.5 km and 1 dBZ, respectively. The two dashed lines indicate the average heights of melting layer.

Fig. 8. Average profiles of (a–b) dBN_w and (c–d) D_m for precipitations over the study regions during the pre-summer rainy-season in 2016–2020.

Fig. 9. Diurnal variations of relative humidity over the study regions derived from ERA5 during the pre-summer rainy season in 2016–2020.

Fig. 10. Conceptual models for the formation of moistest layer over the study region: (a) nighttime and (b) daytime. The blue shadows indicate the vertically moistest layer.

Fig. 11. The same as Fig.9, but for vertical velocity overlapped with equivalent potential temperature θ_e (units: K). Negative vertical velocity indicates updraft. Decreasing θ_e with height indicates conditional instable atmospheric layer.

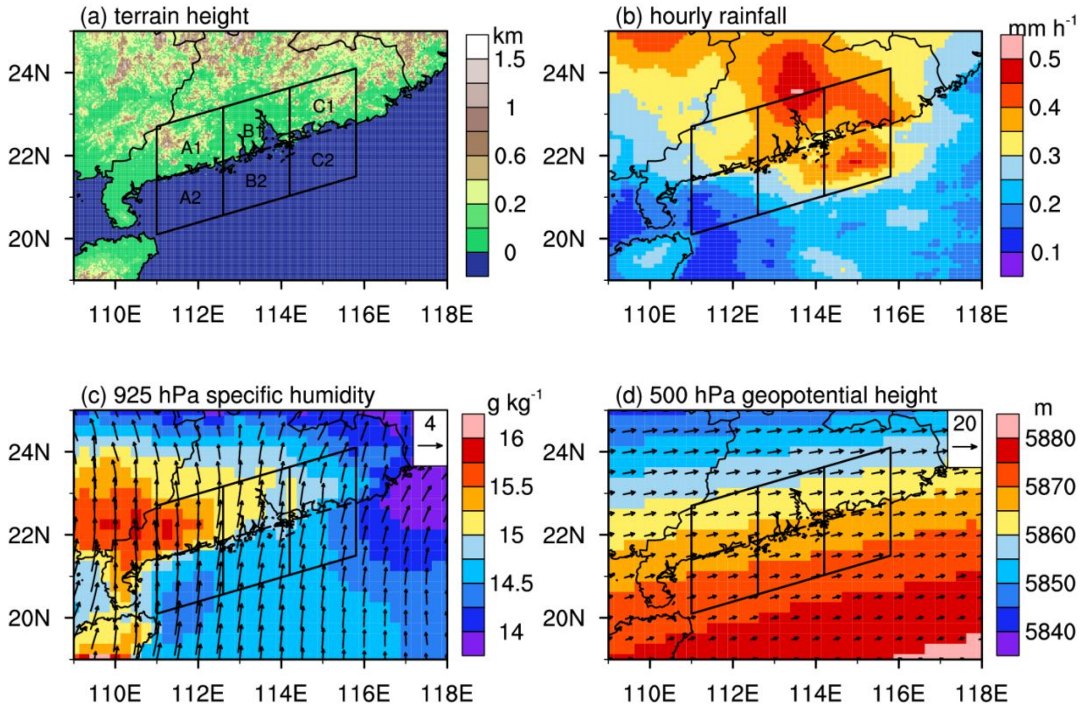

Fig. 1. Average distributions of (a) terrain height, (b) IMERG hourly rainfall, (c) ERA5 925 hPa specific humidity overlapped with wind field, and (d) ERA5 500 hPa geopotential height overlapped with wind field during the pre-summer rainy season (April-June) in 2016–2020. The six parallelograms indicate our study regions.

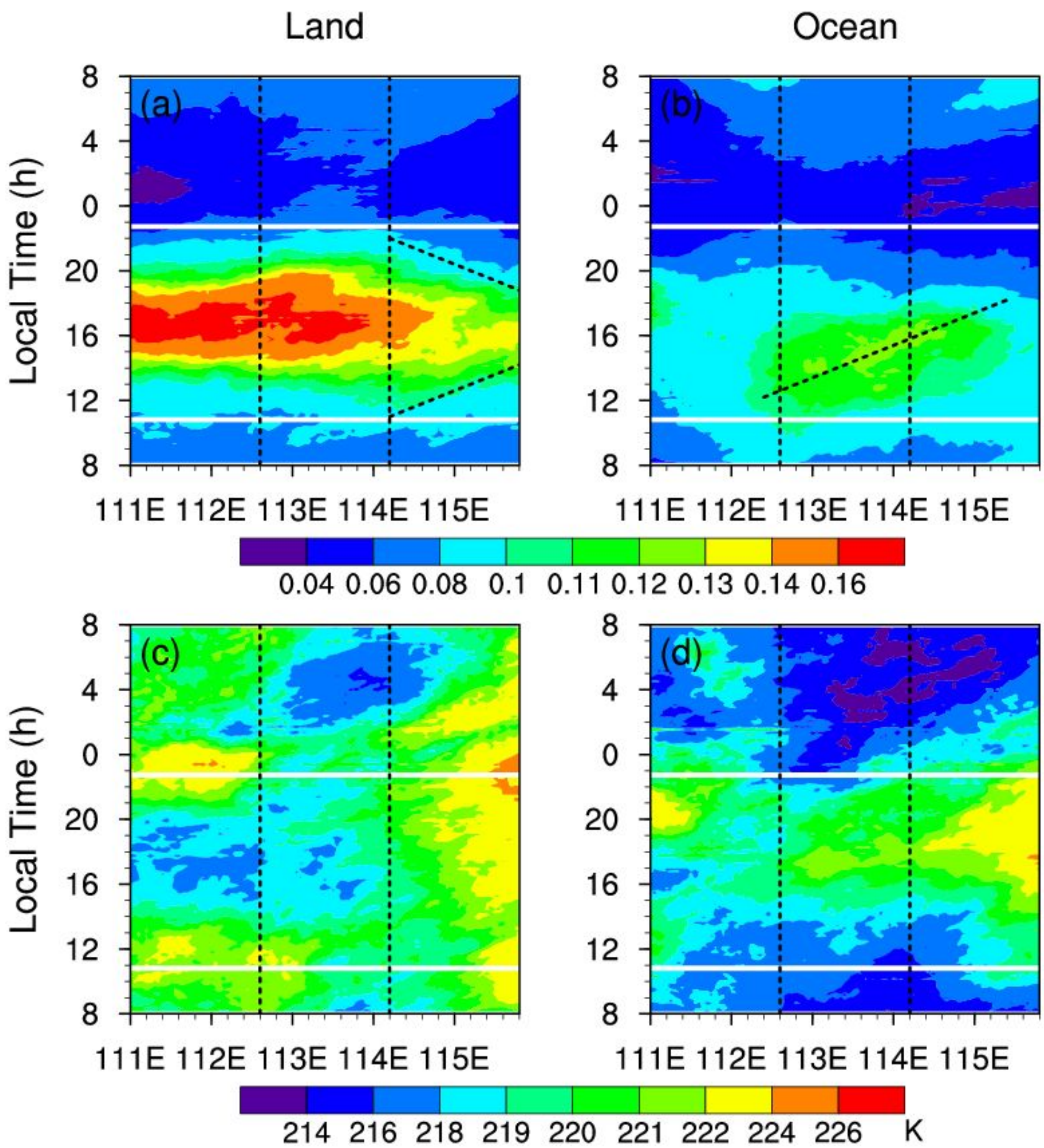

Fig. 2. Diurnal variations of (a–b) MCS frequency and (c–d) brightness temperature of MCS, averaged by latitude over the study regions derived from Himawari-8 AHI. The intervals of time and longitude are 1/6 hour and 0.05°, respectively.

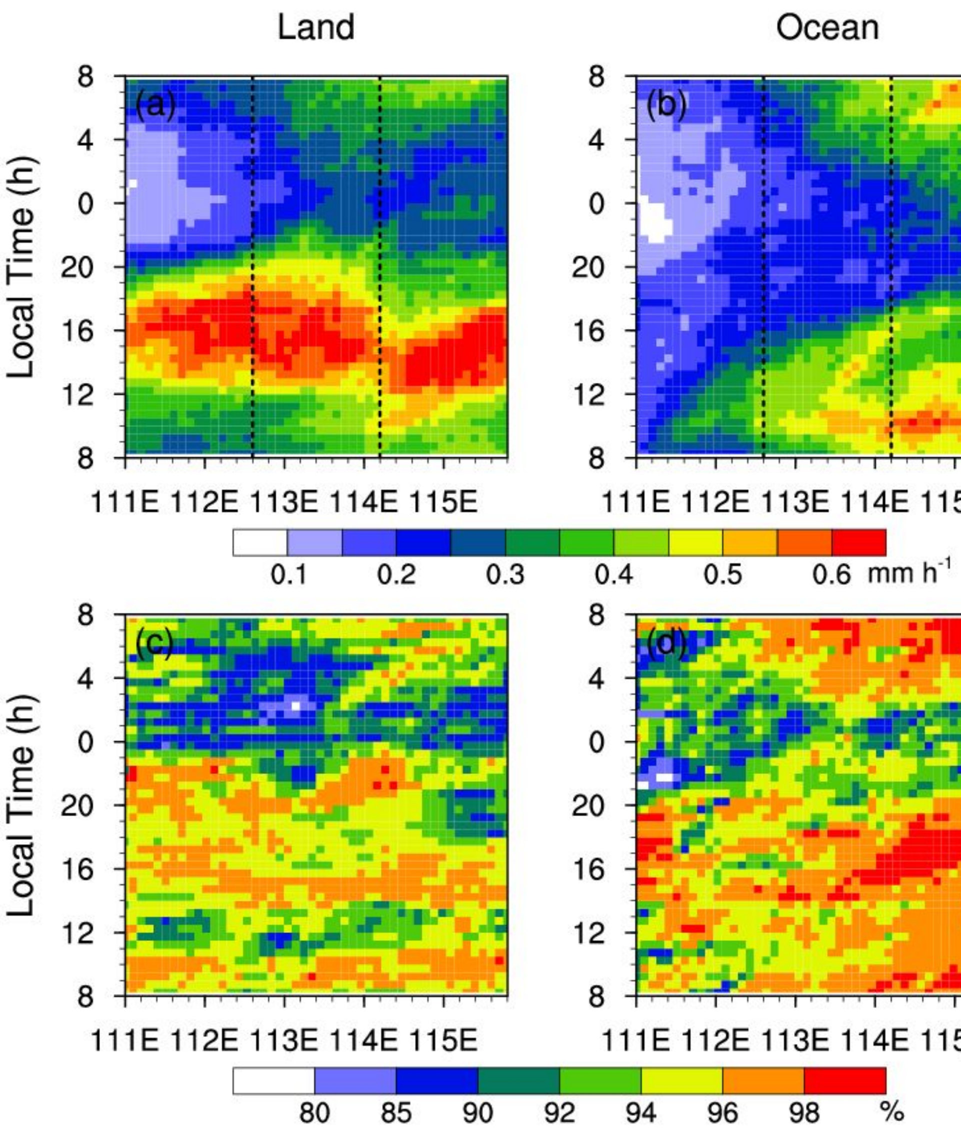

Fig. 3. Diurnal variations of (a–b) total rainfall and (c–d) contribution of MCS to rainfall (attributed to MCS if within 50 km) averaged by latitude over the study regions. The intervals of time and longitude are 0.5 hour and 0.05°, respectively.

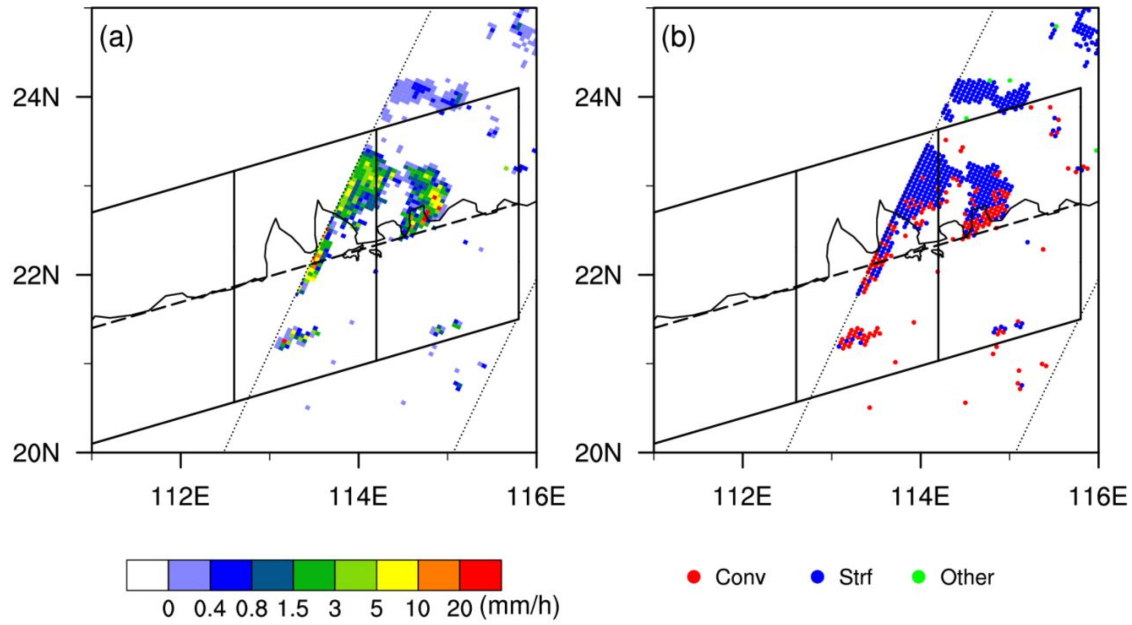

Fig. 4. Horizontal distributions of (a) near-surface rain rate and (b) rain type for an MCS-related precipitation event detected by GPM 2ADPR at 1613 LST, 5 June, 2016.

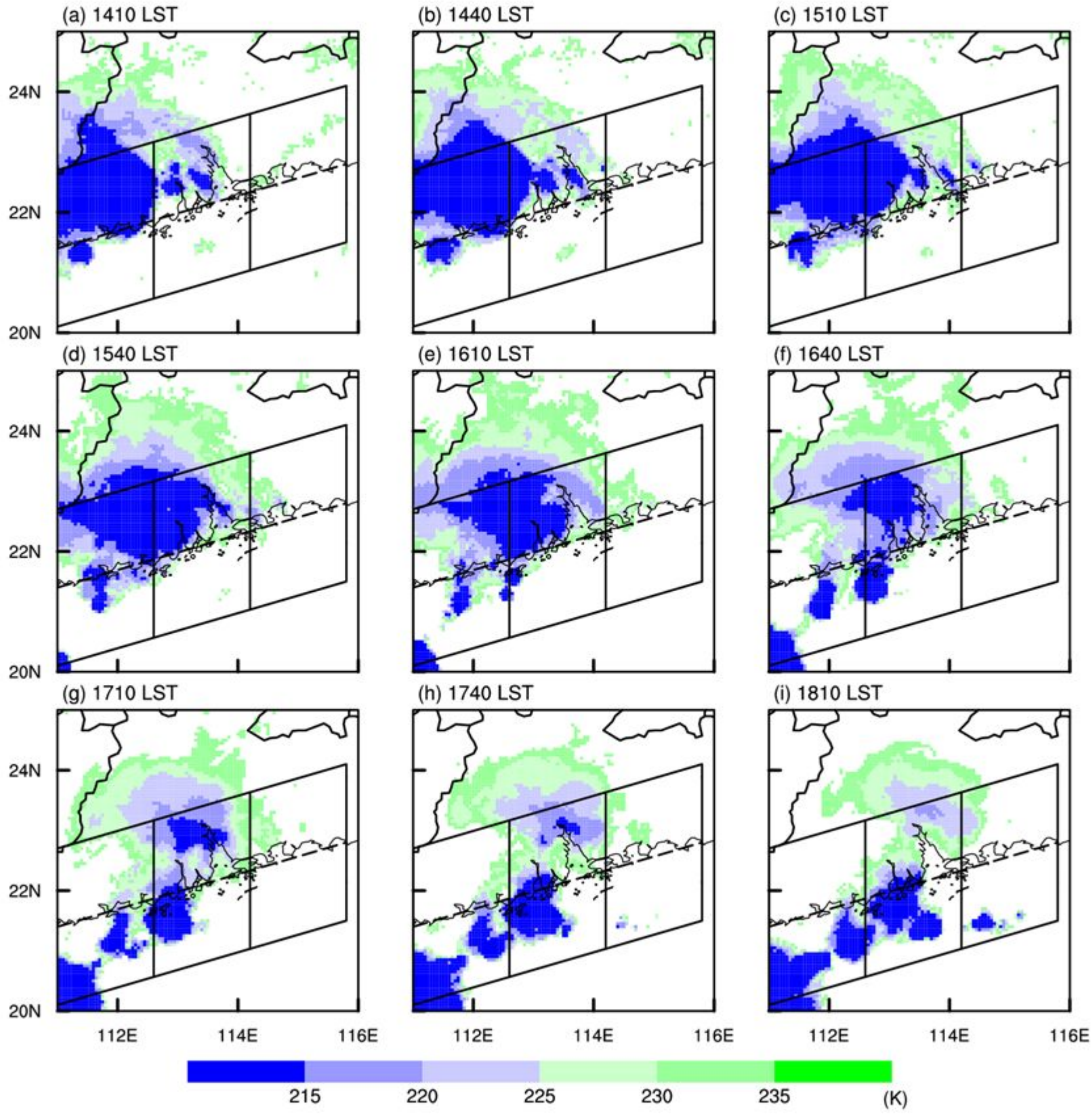

Fig. 5. Hourly distributions of Himawari-8 10.8 μm brightness temperature for the detected event. The DPR precipitation event occurred near the time of panel (e).

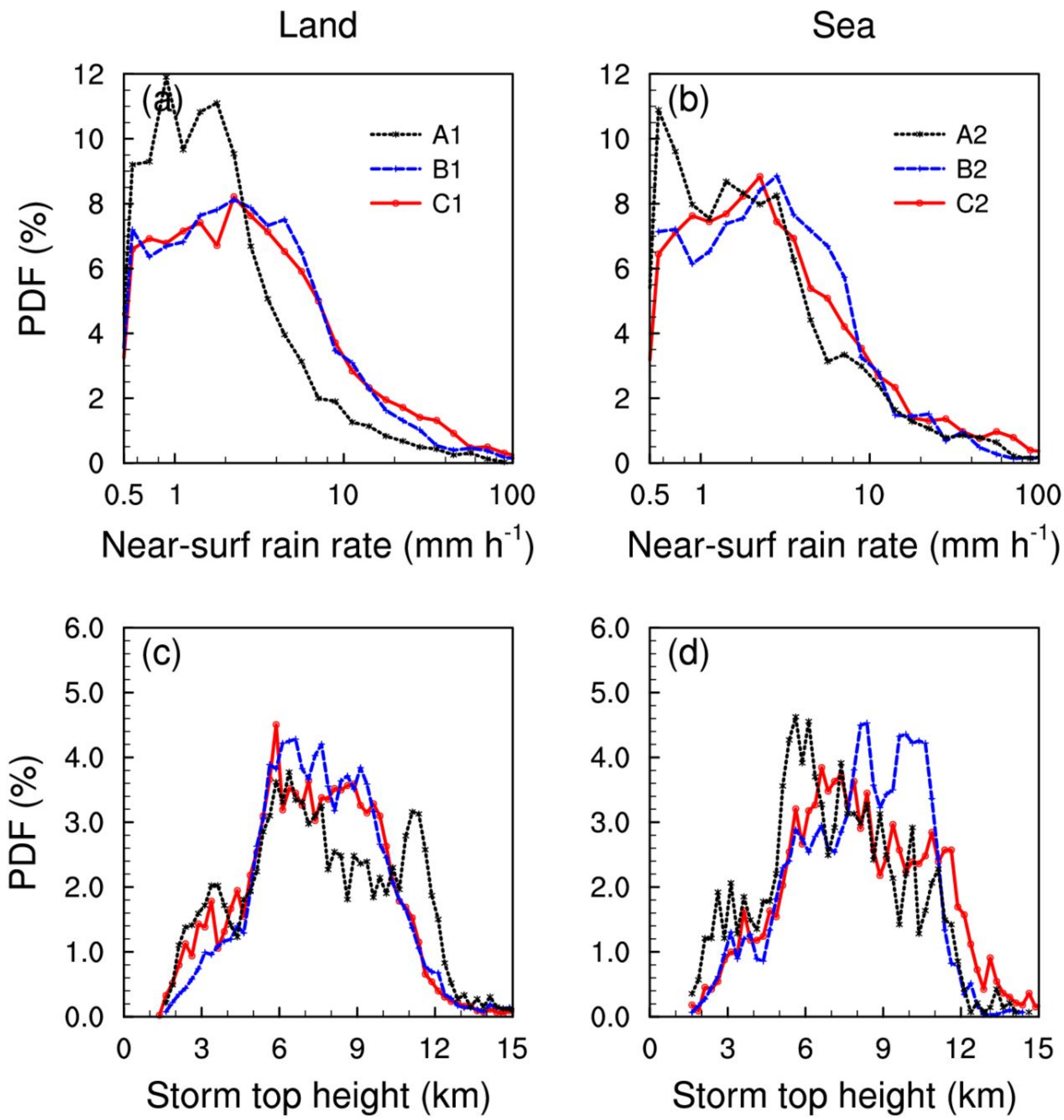

Fig. 6. PDFs of (a–b) near-surface rain rate and (c–d) STH for MCS-related precipitations detected by GPM 2ADPR during the pre-summer rainy season in 2016–2020. The interval of near-surface rain rate is constant in the log coordinate ($\Delta(\lg RR) = 0.1$), and the interval of STH is 0.25 km.

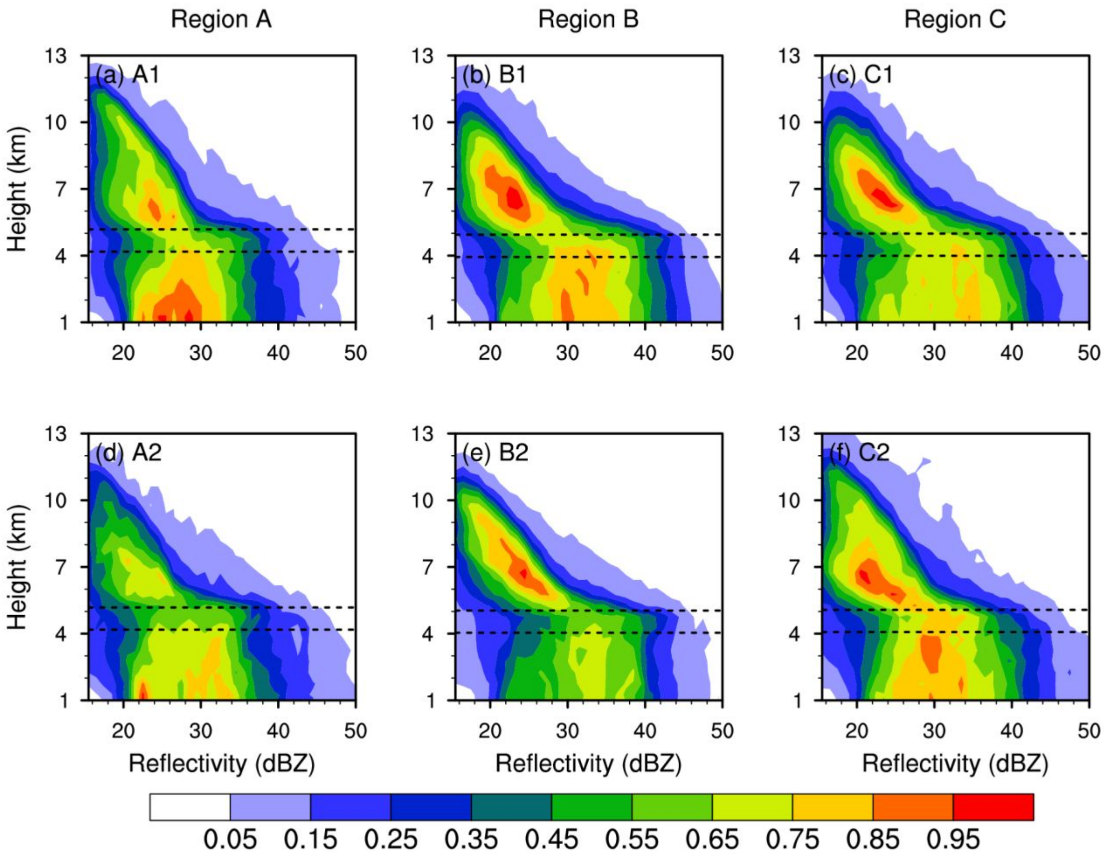

Fig. 7. CFADs of Ku-band reflectivity of MCS-related precipitations over the study regions during the pre-summer rainy season in 2016–2020. The intervals of height and reflectivity are 0.5 km and 1 dBZ, respectively. The two dashed lines indicate the average heights of melting layer.

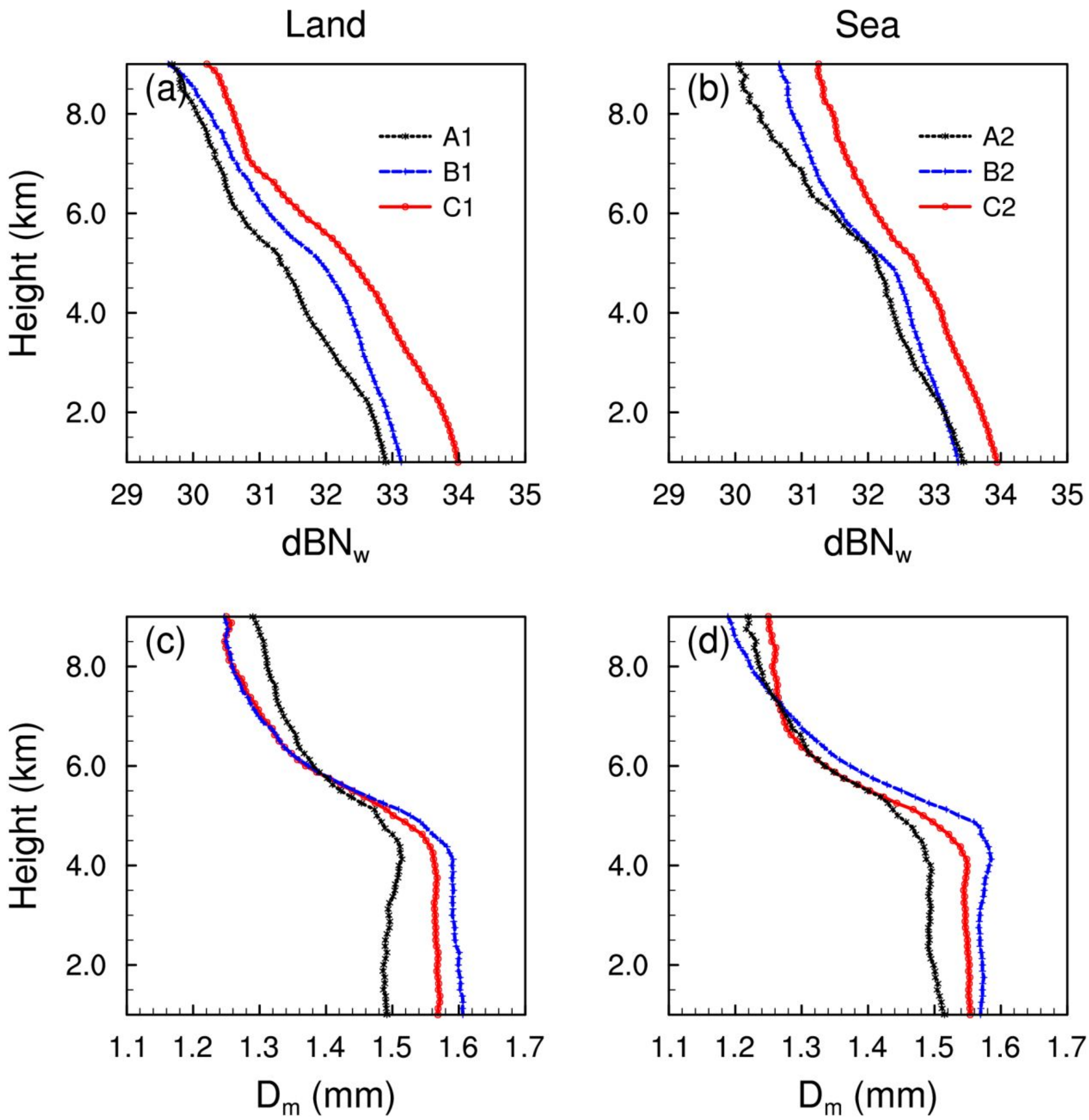

Fig. 8. Average profiles of (a–b) dBN_w and (c–d) D_m for precipitations over the study regions during the pre-summer rainy-season in 2016–2020.

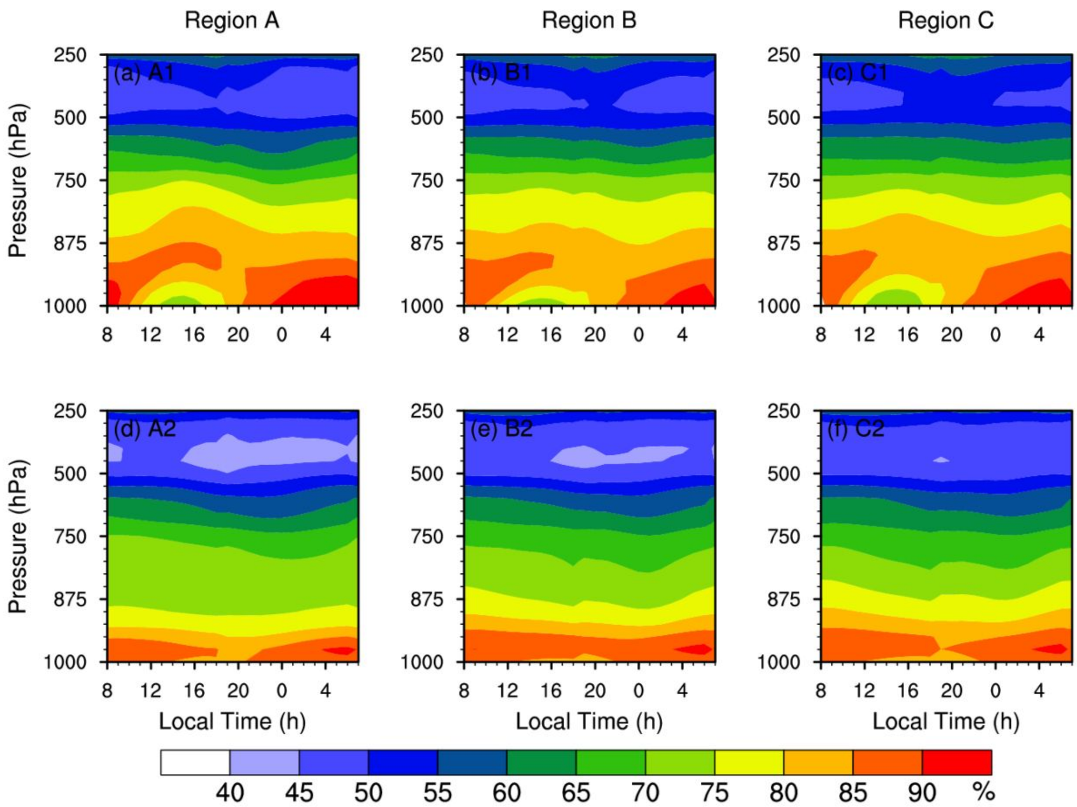

Fig. 9. Diurnal variations of relative humidity over the study regions derived from ERA5 during the pre-summer rainy season in 2016–2020.

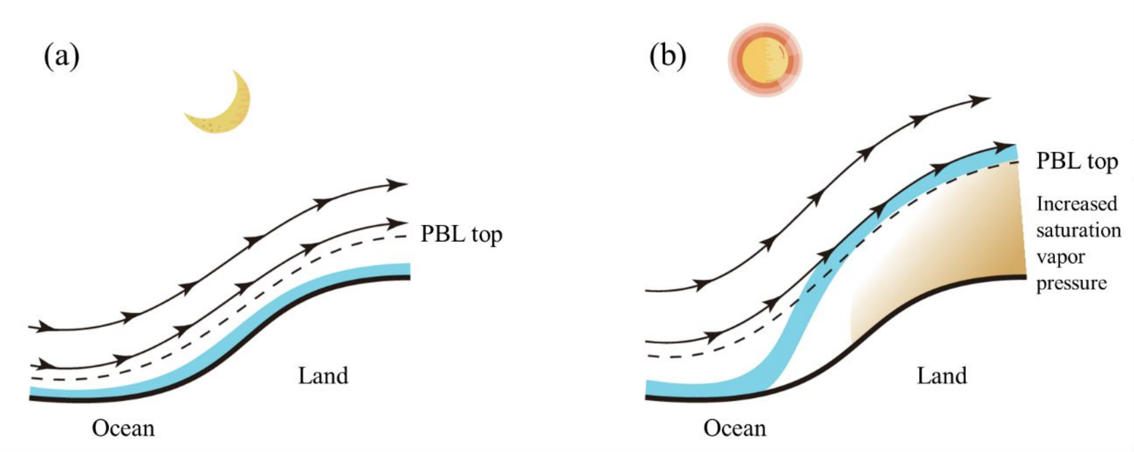

Fig. 10. Conceptual models for the formation of moistest layer over the study region: (a) nighttime and (b) daytime. The blue shadows indicate the vertically moistest layer.

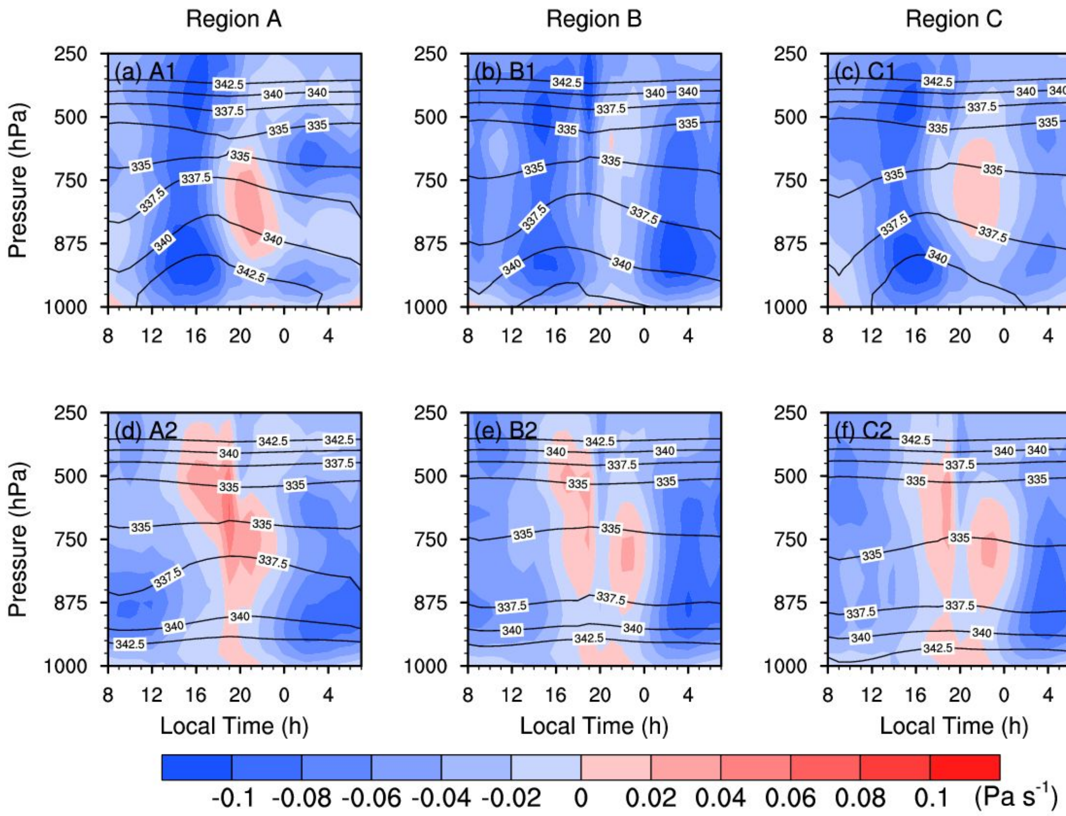

Fig. 11. The same as Fig.9, but for vertical velocity overlapped with equivalent potential temperature θ_e (units: K). Negative vertical velocity indicates updraft. Decreasing θ_e with height indicates conditional instable atmospheric layer.